Acta Materialia 243 (2023) 118499

Contents lists available at ScienceDirect

Acta Materialia

journal homepage: www.elsevier.com/locate/actamat

Microstates and defects of incoherent Σ3 [111] twin boundaries in aluminum

Saba Ahmad, Tobias Brink*, Christian H. Liebscher*, Gerhard Dehm

Max-Planck-Institute für Eisenforschung GmbH, Max-Planck-Straße 1, 40237 Düsseldorf, Germany

ARTICLE INFO

Article history:
Received 7 April 2022
Revised 31 October 2022
Accepted 2 November 2022
Available online 5 November 2022

ABSTRACT

In the last few decades, it has been recognized that a single grain boundary (GB) may exist in several different stable and metastable states, which differ in their atomic structure. However, experimental insights at the atomic structure level are rarely reported. In this study, two different microstates of incoherent Σ3 [111] ($11\bar{2}$) GBs from two different orientation relationships (ORs) in an aluminum thin film grown on sapphire, comprised of slightly different structural units, are reported. The structural units in ORII exhibit hexagonal units while in ORI the hexagonal units are slightly distorted. Molecular statics simulations are utilised to understand the difference in excess properties of both states, which suggest that strain could potentially contribute to the stability of the ORII GB microstate over the ORI microstate. In addition, the atomic structure of the two ORs along the ⟨110⟩ zone axis reveal the rigid body microscopic translations of different magnitude of {111} planes across the GB experimentally. Furthermore, in the case of asymmetric variants of the same GBs, different types of Σ3 [111] disconnections with Burgers vectors ($\mathbf{b}_1 = 1/6[\bar{1}\bar{1}2]$), ($\mathbf{b}_2 = 1/2[\bar{1}01]$) and varying step heights ($h = 2a_{dsc}$, $5a_{dsc}$) are investigated and their implications on the GB mobility are discussed.

1. Introduction

Most engineering materials are polycrystalline in nature and are composed of a 3D network of grain boundaries (GBs) spread throughout the material. GBs are fully characterized by five macroscopic degrees of freedom (DOF). Three of them specify mutual misorientation of the two adjoining grains and two of them specify the orientation of the GB plane between the two crystals [1]. However, the atomic structure of the GB is not fully described by these five macroscopic DOFs. Several studies reveal the existence of multiple stable and metastable states for a GB with fixed macroscopic DOFs, characterized by distinct thermodynamic excess properties [2–8]. A large number of possible microscopic rigid-body translations in the GB plane give rise to the different atomic structures of the GBs [9–12]. Due to this, these states have been called GB phases [13] or complexions [7,14–16]. In analogy to bulk phases, the transitions between these GB phases can be described using the GB excess free energy, which is a function of the thermodynamic excess properties [17,18]. The GBs' distinct atomic nature controls their properties, which in turn have an impact on various material processes, such as recrystallization, grain growth and the plasticity of nanocrystalline materials [19–21]. Therefore, a detailed investigation of the GB structure and its influence on the GB properties is imperative for a fundamental understanding of the GBs to design novel materials. Numerous atomistic computer simulation studies [22–24] have been carried out to investigate the structure and energy of various tilt GBs in pure component systems, but mainly for the [001] or [011] tilt axes. However, the experimental and theoretical atomic structure of [111] tilt GBs in pure Al has barely been studied.

The notion of GB disconnections, which are line-defects exhibiting both dislocation and step character in grain or phase boundaries was first proposed and developed by Bollman in 1970 [25–28]. The creation and dynamics of disconnections plays a vital role in various GB kinetics, such as GB migration via lateral motion of disconnections along GBs [29], disconnection movement during GB sliding [30] and deformation coupled GB motion [31]. Recently, Zhu et al. [32] investigated the atomistic migration mechanism of the Σ11 (113) coherent GB and demonstrated experimentally that the frequent coalescence and dissociation of the two disconnections with the height of either one or two atomic layers contribute to GB migration. The GBs' properties and macroscopic behavior are highly controlled by the atomic structure of the disconnections. Therefore, we need direct experimental evidence of

* Corresponding authors.
E-mail addresses: t.brink@mpie.de (T. Brink), liebscher@mpie.de (C.H. Liebscher).

https://doi.org/10.1016/j.actamat.2022.118499

the local atomic structures of these defects present at the GB to discern their impact on the interfacial properties.

In this study, efforts have been made to establish a direct correlation between the atomic structure of different structural states of Σ3 [111] tilt GBs and their effect on excess properties by using aberration corrected scanning transmission electron microscopy (STEM) techniques in combination with molecular statics and density functional theory simulations. STEM investigations revealed that despite possessing the same macroscopic degrees of freedom, two different microstates of the Σ3 [111] {211} GBs exist in Al. The simulations showed that the two microstates could emerge from different local stress or strain states present at the interfaces, which result in differing interfacial excess properties. Furthermore, different types of structural defects are explored in two orientation relationships (ORs) between the film and the substrate and their implications are discussed.

2. Methods

2.1. Experimental details

Pure Aluminum thin films investigated in this study were grown by physical vapor deposition technique on a 2 inch (0001) oriented sapphire wafer. Film deposition was carried out at the Central Scientific Facility for Materials of the Max Planck Institute for Intelligent Systems in Stuttgart under ultra-high vacuum conditions, followed by a post deposition annealing for several cycles at 400 °C at the rate of 6 K/h in Argon atmosphere. Firstly, the sapphire substrate was Ar-sputter cleaned at 200 eV to remove the surface contaminants in the UHV system and then annealed at 800 °C for 2 h to further remove structural defects. Subsequently, the substrate was cooled down to 100 °C and the Al films were sputtered with a deposition rate of 0.11 nm/s. Finally, the sample was slowly cooled down to room temperature in vacuum. The nominal film thickness was chosen to be 800 nm.

The microstructural attributes (grain orientation, grain size, CSL GB type and its distribution) of the thin film were characterized by using electron backscatter diffraction (EBSD) at 20 kV in a JEOL JSM-6490 scanning electron microscope (SEM). EBSD data analyses were performed with the help of OIM 7.0 software. Firstly, the mistilt in the EBSD dataset was rectified by utilizing the center peak of the Al {111} pole figure. Thereafter, EBSD analysis was performed on the dataset to get rid of the noise by utilizing the following parameters: elimination of data points with a confidence index (CI) value below 0.1, grain tolerance angle of 5°, and neighbor CI cleanup was performed on data points with CIs below 0.3–0.4. In total, seven (plan view and cross sectional view) site-specific TEM specimens from the thin film (pre-analyzed by EBSD) were lifted out in a dual-beam SEM/focused ion beam instrument (Helios Nanolab 600i, Thermo Fisher Scientific) having Xenon as an ion source. Using Xe-FIB instead of conventional Ga-FIB avoids the problem of implanted Ga, which tends to segregate to the Al GBs and thus lead to very prompt, substantial loss of Al ductility via liquid metal embrittlement [33]. A redesigned procedure of wedge milling approach, described by Schaffer et al. [34] was adapted for the thinning of the lamella. Exact milling parameters depending on each sample are listed in Table 1, depicting a typical thinning procedure. In principle, for coarse milling/thinning the FIB was operated at 30 kV, for gentle thinning at 16 kV and 8 kV from ∼1000 nm down to ∼200nm thickness followed by final polishing at 2 kV, whereby the beam current was varied from high to low for each kV. In the current work, conventional TEM characterization was primarily carried out at the Thermo Fisher Scientific Titan Themis 80–300 X-FEG TEM. BF imaging was used to investigate the cross-sections of both the ORs present in the Al thin film. Selected area diffraction (SAD) and high-resolution transmission electron microscopy (HRTEM) were used to determine the orientation of Al grains w.r.t the sapphire substrate.

Table 1
Plasma (Xe) FIB operating parameters applied for the thinning of plan-view TEM lamella.

Lamella thickness	Ion accelerating voltages, relative tilt, ion beam current(s)
Coarse thinning (∼ 1200nm)	30 kV, ± 0.5°, 0.10 nA
∼ 1000 nm	16 kV, ± 1°, 0.30 nA - 0.10 nA
∼ 800 nm	16 kV, ± 1.5°, 30 pA - 10pA
∼ 200 nm	8 kV, ± 2°, 10 pA
Final polishing	2kV, ± 4°, 5pA - 4 pA

All STEM images in high-angle annular dark field mode (HAADF-STEM) were acquired using a C_S-probe corrected Titan Themis 60–300 (Thermo Fisher Scientific), equipped with a gun monochromator and operated at 300 keV with a probe current of about 70 to 90 pA. In order to avoid a thick amorphous layer on the Al free surface from the sample preparation, slightly thicker (∼70 to 90 nm) PFIB lamellas are employed for STEM measurements. Hence, the operating voltage of 300 keV is used with the aim to obtain better contrast and resolution. The semi-collection angles of the annular detector for HAADF imaging were set to 40 mrad/78 mrad – 200mrad using a semi-convergence angle of 17 mrad. Furthermore, in order to reduce the effect of instrumental instabilities such as drift and noise in the images, image series comprising of 10–40 images with a dwell time of 2–20 μs were recorded and averaged.

2.2. Atomistic simulation

In order to analyze the thermodynamic properties of the grain boundary structures in more detail, we also simulated them using an embedded atom method (EAM) potential for Al [35] using the LAMMPS software [36]. We calculated the 0 K cohesive energy and lattice constant for the fcc structure. To prepare the GB structure search, we constructed a bicrystal with the following crystal directions along the Cartesian directions: [111], $[1\bar{1}0]$, and $[11\bar{2}]$ for the first crystallite and [111], $[0\bar{1}1]$, and $[2\bar{1}\bar{1}]$ for the second one. The tilt axis was therefore aligned in x direction and the GB normal in z direction. The crystallites were joined at their {112} surfaces and the system had periodic boundaries in x and y direction and open boundaries in z. The final boxes had a size of around $14 \times 17 \times 120$ Å^3 with 1440 atoms. The 0 K structures were found by displacing one crystallite with regard to the other with constant simulation box size and optimizing the atomic positions with regard to the potential energy (γ-surface method). Thermodynamic excess properties were calculated as described in Refs. [17,18] and excess shears as described in Ref. [8].

3. Results and discussion

3.1. Microstructural characterization of thin films

Fig. 1 shows a schematic of the geometry of the Al thin film on the sapphire substrate including the corresponding crystallographic directions.

Fig. 2 summarizes the microstructural attributes of the epitaxial Al thin film, especially texture, grain size, GB character and their distributions obtained by EBSD in the SEM.

EBSD studies revealed a strong ⟨111⟩ texture in the Al film as shown by the {111} Al pole figure and IPF map (in the normal direction). The central peak of the {111} Al EBSD pole figure corresponds to (111) Al planes that are parallel to the film surface. In accordance with the literature [37,38] on vacuum deposited fcc metallic thin films, the {111} texture can be associated with the

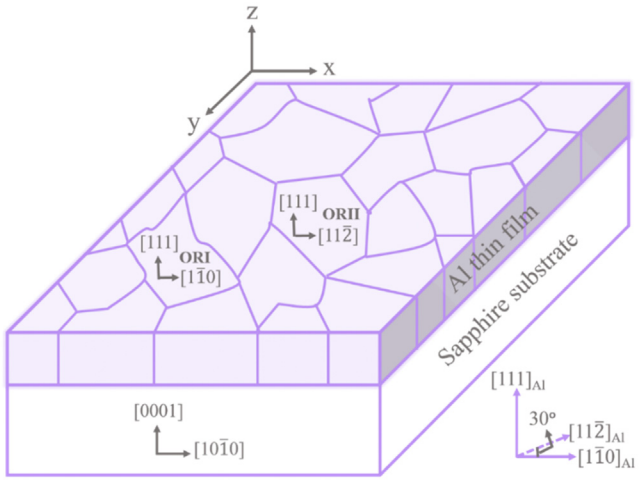

Fig. 1. Schematic of the Al thin film grown on the sapphire substrate including corresponding crystallographic directions (for both ORI and ORII). The *z*-axis represents the out of the plane direction, i.e. [111], while *x*-axis and *y*-axis represent the in-plane directions. The in-plane directions for ORI and ORII are [1$\bar{1}$0] and [11$\bar{2}$], respectively, in the Al film.

tendency towards minimum energy configuration, i.e. corresponding to the lower surface energy planes. The existence of two orientation relationships (OR I and OR II) between Al and Al_2O_3 – containing two twin-related growth variants rotated by 180° for each OR – is designated by the six other (111) peaks in pole figure. ORII corresponds to a 30° rotation of Al crystallite around the ⟨111⟩ direction with respect to underlying (0001) oriented sapphire [39]. A 30° misorientation between OR I and OR II grains is anticipated from the angle between ⟨10$\bar{1}$0⟩ α-Al_2O_3 (ORI) and ⟨2$\bar{1}\bar{1}$0⟩ α-Al_2O_3 (ORII). Both the ORs are described as follows:

ORIa/**b** $\{111\}\pm < 0\bar{1}1 > \mathrm{Al} \,||\, (0001) < 10\bar{1}0 > \alpha - Al_2O_3$

ORIIa/**b** $\{111\}\pm < 0\bar{1}1 > \mathrm{Al} \,||\, (0001) < 2\bar{1}\bar{1}0 > \alpha - Al_2O_3$

It is important to note that in the (111) pole figure, sharp diffraction peaks are observed for both OR I twin variants. Conversely, less sharp peaks are observed for OR II with an angular deviation of ±8° (see the pole figure in Fig. 2b)). The corresponding CSL boundaries and their distribution are shown in Fig. 2b). The microstructure of the film is mainly dominated by high angle boundaries. Among 62% of all CSL boundaries, approximately 38% are Σ3 twin boundaries followed by 11% Σ13b, 6% Σ7, 2% Σ19b, 2% Σ21a, 1.5% Σ37c and a very small percentage of other higher-order CSLs. The remaining percentage of the GBs in the film are low angle boundaries.

3.2. Atomic structure of Σ3 grain boundaries with ORI and ORII

Representative atomic resolution images of symmetrical Σ3 twin boundaries from the two different ORs are presented in Fig. 3. The two adjacent grains are oriented along the [111] axis with a grain misorientation of 60° for ORI and 59° for ORII, with a GB habit plane of (11$\bar{2}$). Due to the larger change in GB curvature locally in ORII, frequent changes in GB plane inclination lead to

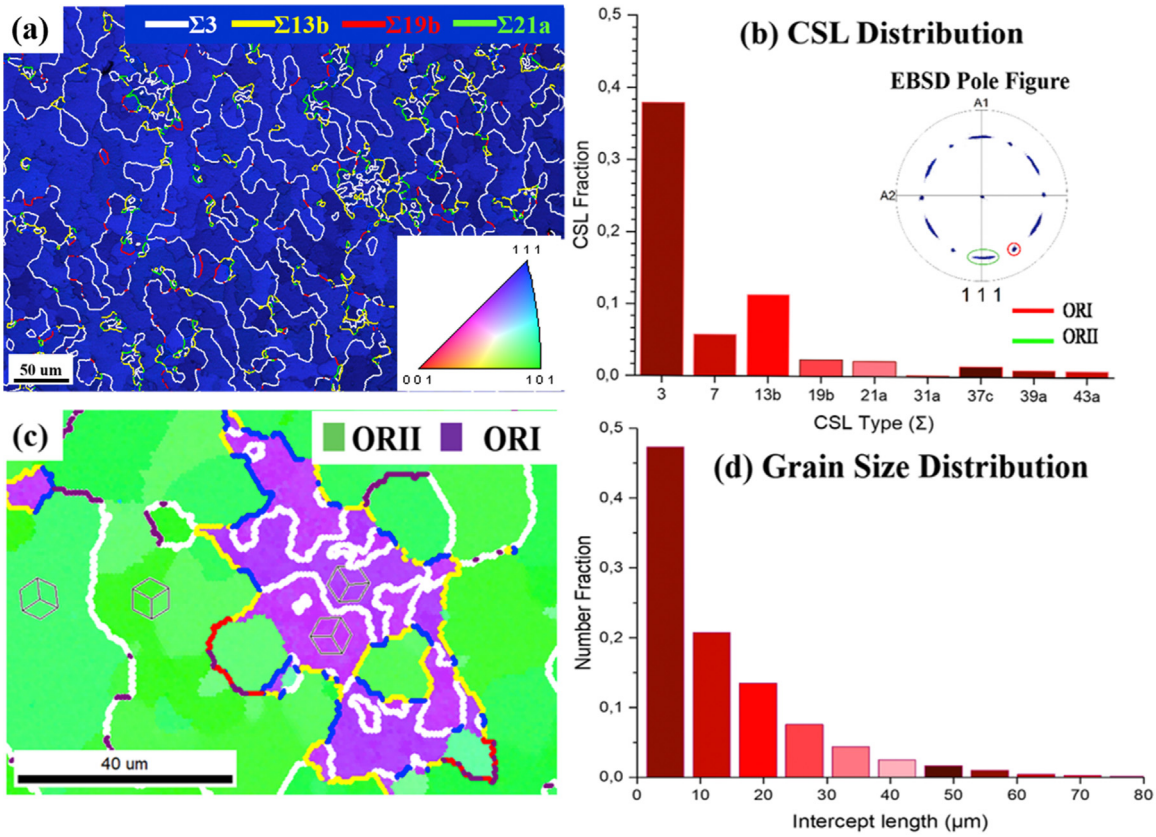

Fig. 2. EBSD results for the Al thin film on a sapphire substrate. a) The inverse pole figure map in [111] direction. Blue color indicates {111} planes that are parallel to the surface. The colored lines indicate different [111] tilt GB types in the film. **b)** Relative occurrence of CSL boundaries. The inset shows a {111} Al pole figure of the deposited film generated from EBSD data with OR I a/b and OR II a/b marked. **c)** The inverse pole figure map in transverse direction represents the grain orientation, shown by superimposed cubes. ORI and ORII are shown in purple and green, depict the twin variants. Σ3 twin boundaries are illustrated in white, Σ7 GBs in blue, Σ13b GBs in yellow and Σ19b in red and further CSL boundaries of higher order in blue. **d)** Distribution of grain sizes in the film.

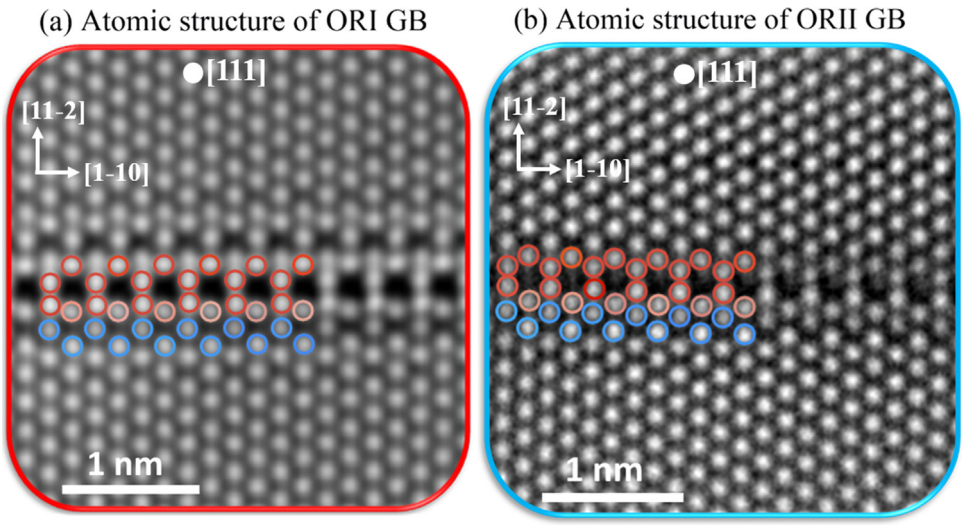

Fig. 3. STEM-HAADF images showing the atomic-resolution details of incoherent symmetric Σ3 grain boundaries viewed along the [111] zone axis. a) Atomic structure of symmetric Σ3 $(11\bar{2})$ from ORI. **b)** Atomic structure of symmetric Σ3 $(11\bar{2})$ from ORII. The red coloring of the atomic columns serves to highlight the structural units. The blue colored atoms highlight the motifs in the cross-sectional view of the GB (see Fig. 5 and 6). Both the images were filtered using Wiener filter with the following parameters: Highest frequency = 80 and edge smoothing = 5%.

steps or facets in the GB. This is also demonstrated microscopically in Figure S4 and S5 by using plane trace analysis in EBSD and in Fig. 8 (to be discussed in the upcoming Section 3.5) by using BF-TEM imaging. Fig. 3 shows straight, symmetric segments, which occur in between the steps. The structural unit (SU) model is utilized to describe the complete structure of the Σ3 $(11\bar{2})$ GB. On closer inspection, it is found that despite having the similar macroscopic degrees of freedom, the characteristic structural units of Σ3 for both the ORs are slightly different from one another. The Σ3 $(11\bar{2})$ structure from ORI, is comprised of sub-units as highlighted by red circles in Fig. 3a). In the projection, the red sub-unit possesses a distorted hexagon shape with no mirror symmetry across the GB. In accordance with the terminology of the SU model, the GB structure can be written as |E| for the Σ3 $(11\bar{2})$ from ORI, where E represents the distorted hexagon unit. The vertical lines represent one GB period (unit cell at the GB) along the direction of the GB plane.

In contrast, the Σ3 structure from ORII consists of red sub units that appear moderately different from the |E| units. It exhibits a perfectly hexagonal shape, which appears mirror symmetrical in the projection, and can be written as |E'|, where E' represents the perfect hexagon unit. The SUs from two different ORs are also compared quantitatively by measuring geometrical features (atomic distances and angles subtended by the sides of the hexagon) of the units. The methodological error in measuring these angles and the atomic distances between the atoms is far smaller than the difference in the actual values from the two structures.

It is evident from the measurements that the angle α (as defined in Fig. 4) in the distorted hexagon (|E| units) is around 29° larger than in the perfect hexagon (|E'| units). A large change in the α angle also results in slight shifts in the atomic positions of the surrounding atoms at the GB as can be seen in the supplemental Figure S3.

3.3. Cross-sectional view of the Σ3 GBs

A conventional BF-TEM image of the cross sectional view of the Σ3 GB from OR I in Fig. 5a) illustrates that the boundary is straight from the substrate to the surface of the film and does not contain any facets. The Al film thickness is determined to be 805 nm, approximately. STEM-HAADF images in Fig. 5b)–e) represent the atomic structure of the boundary from the regions marked by the green, light blue, black and dark blue rectangles in Fig. 5a). An interesting feature is the shift between the {111} planes at the GB: There is no such translation present at position A, which is very close to the sapphire substrate. As we move farther away from the substrate, it increases gradually up to approximately 0.69 Å near the surface of the Al film.

A conventional BF-TEM image of the cross-section specimen of the Al film containing a Σ3 GB with ORII is shown in Fig. 6a). The boundary appears to be mostly straight but with the incorporation of two asymmetric facets with GB plane {122} / {100} inclined towards the right grain, marked by a pink rectangle in the image. These facets are named asymmetric facet 1 and asymmetric facet 2. It seems that the boundary moves to the right during annealing at elevated temperatures. The atomic structures at position A and B consist of the same triangular units along the GB as observed in ORI. Furthermore, the facets also consist of triangular units from the {211} symmetric twin with the incorporation of some additional units (Fig. 6d)), having either one or two atomic planes to accommodate the deviation in GB plane from the symmetric inclination.

3.4. Atomistic simulation

At this point, it is still unclear if the |E'| unit is simply an elastically distorted version of the |E| unit, or a more clearly delineated microstate. We could find the |E| motif at 0 K and without externally applied stress or strain using the γ-surface method as described in Section 2.2 (Fig. 7a)). The |E'| variant could not be found.

In the experiment, the film is grown on a sapphire substrate, which can lead to residual strains (the possible sources of these strains are discussed later). Here, we assume that this corresponds to an isotropic strain in the *yz* plane ($\varepsilon = \varepsilon_{22} = \varepsilon_{33}$), i.e., the plane that is parallel to the substrate in the experiment, and open boundaries in the direction normal to the substrate (plane stress condition with $\sigma_{11} = 0$). Unfortunately, the plane stress condition leads to significant size effects, yielding different results for different ratios of GB volume vs. bulk volume [17]. We therefore utilized plane strain conditions ($\varepsilon_{11} = 0$) and verified that the results are unaffected by varying ε_{11} (Supplemental Figure S7). Due to the boundary conditions, we can furthermore only apply a stress nor-

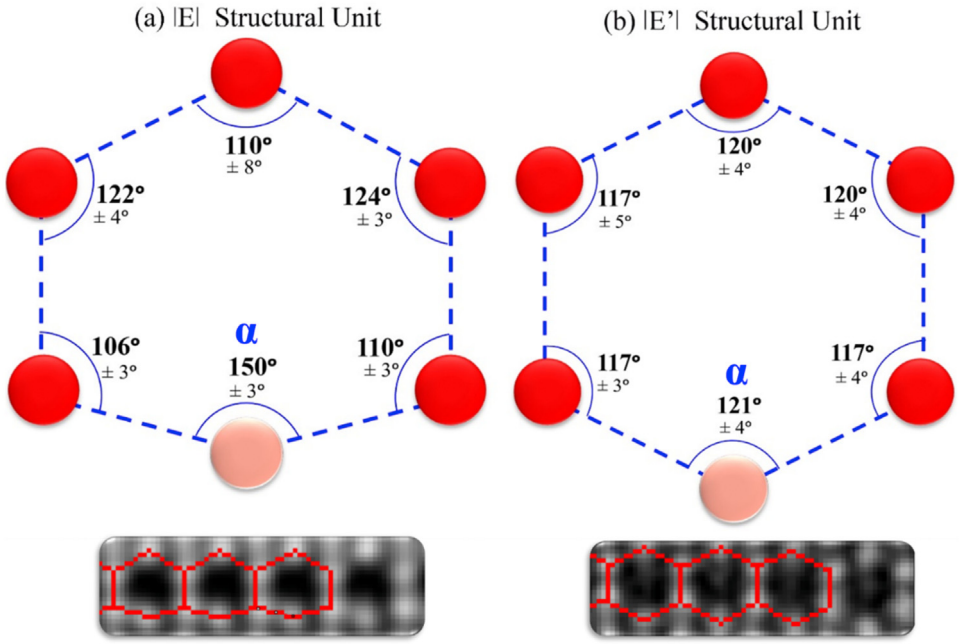

Fig. 4. Schematic illustration of the projection of two different structural units of incoherent symmetric Σ3 grain boundaries from two ORs. a) Distorted hexagon units (|E| units) from ORI. **b)** Perfect hexagon units (|E'| units) from ORII. Images at the bottom show the experimental images of the structural units. The different values of angle α depicted in **c)** and **d)**, indicate a slight shift in the atomic position of the light red atomic column in the structural units.

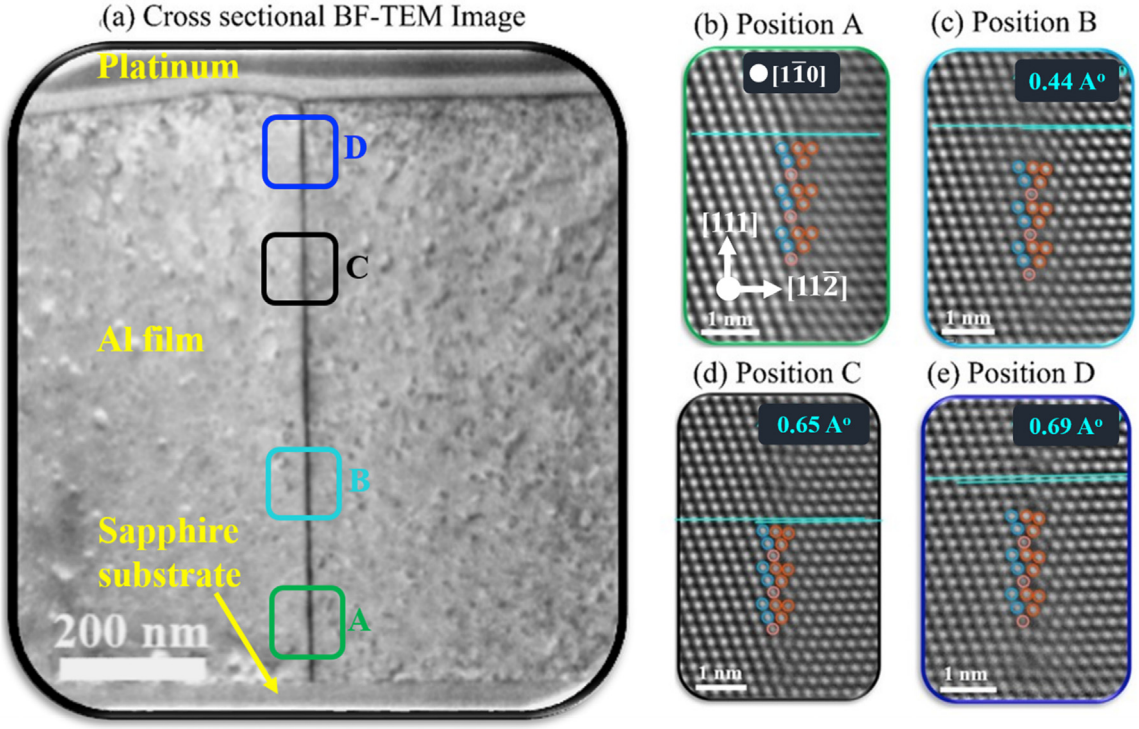

Fig. 5. Cross-sectional view of the Σ3 (11$\bar{2}$) GB from ORI along ⟨110⟩ zone axis. a) Conventional BF-TEM image of the cross-section of Σ3 GB from ORI. STEM-HAADF images in **b)-e)** represent the atomic structure of the boundary marked by green, light blue, black and dark blue rectangles in **a)**. Translation of {111} planes across the GB is increasing gradually from the bottom near the substrate to the surface of the Al film.

mal to the GB (σ_{33}) and a strain (ε_{22}) in y direction without introducing size effects in a bicrystal setup [17]. In order to be able to apply a plane strain, we therefore computed the stress–strain relation of a similarly sized and oriented defect-free fcc slab and used this to estimate the stress needed to obtain a given ε_{33}.

At a strain of around 0.5%, we observe a transition from the |E| to the |E'| structure (Fig. 7b)). Additionally, at each applied strain value, we could only observe one of these two structures, while the other one was always unstable and transformed immediately. That means that neither structure can exist in a metastable state.

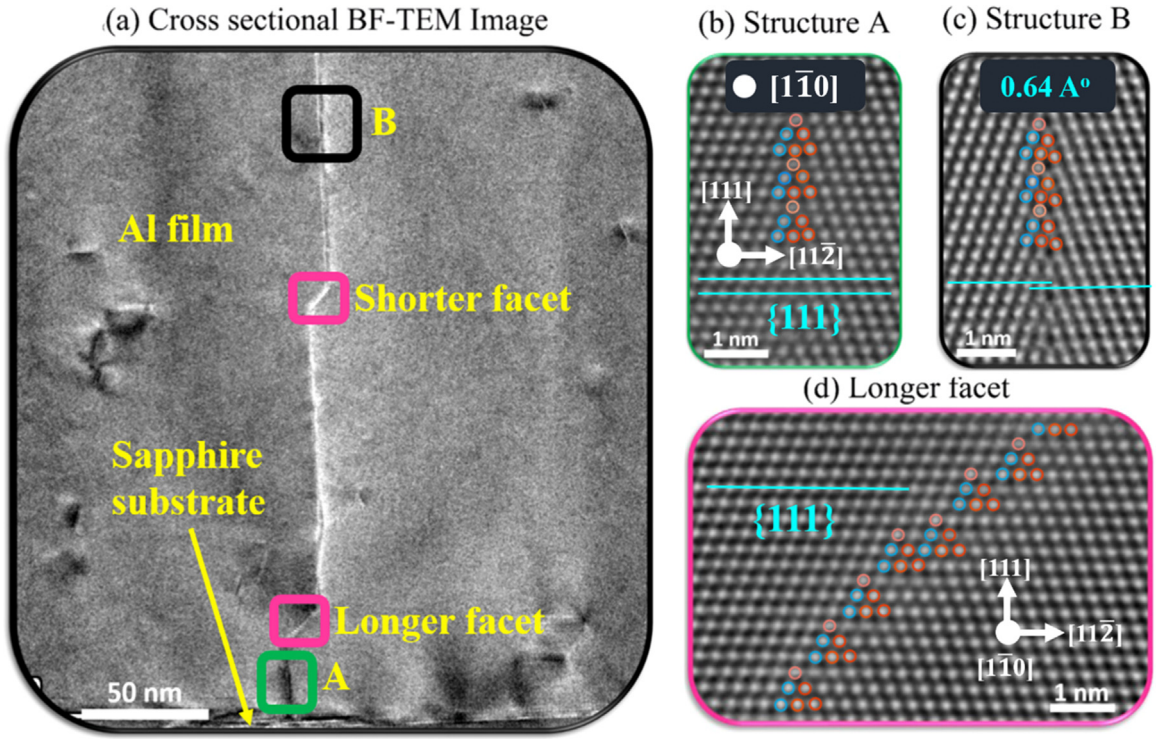

Fig. 6. Cross-sectional view of the Σ3 (11$\bar{2}$) GB from ORII along ⟨011⟩ zone axis. a) Conventional BF-TEM Image of the cross-sectional of Σ3 GB from ORII. STEM-HAADF images in **b)** and **c)** represent the atomic structure of the boundary marked by the green and black rectangle in **a). d)** Magnified view of the pink rectangle highlights the atomic structure of the asymmetric twin facet (122)/(100) with no rigid body translation of {111} planes but includes other structural units. For Σ3 (11$\bar{2}$), different microscopic rigid body translations are found along the boundary as shown in **b)** and **c).**

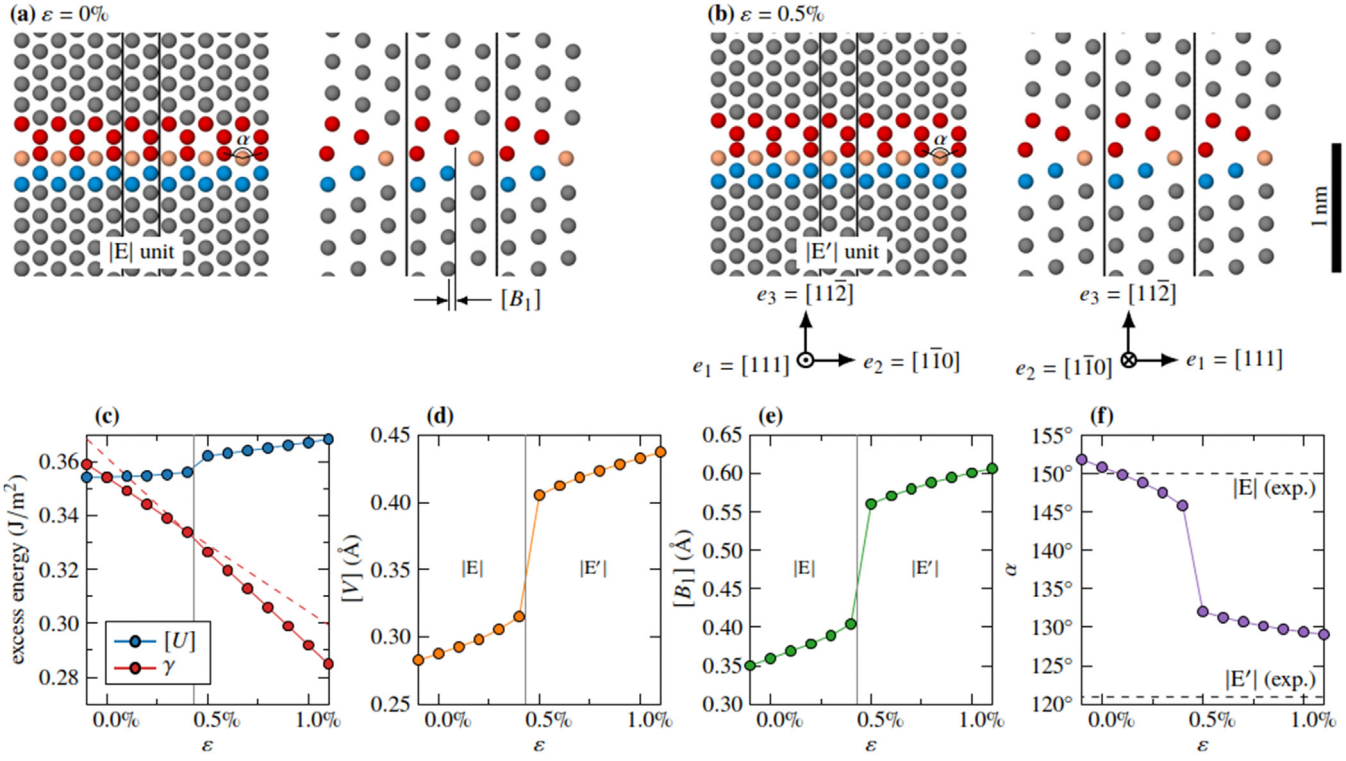

Fig. 7. Simulation of the two different motifs |E| and |E'| observed in the experiment. a) In the stress and strain-free state, the |E| unit can be found. **b)** The |E'| unit appears when applying a strain of 0.5%. The coloring in the images highlights the structural units. The atom indicated in light red color shifts its position when transforming from |E| to |E'| units, leading to a change in the angle α when viewed in the projection from the [111] direction. c)–f) The GB excess energy $[U]$, excess free energy γ, excess volume $[V]$, excess shear $[B_1]$ along the tilt axis are shown together with the angle α. A clear jump in these properties marks the transformation between the two motifs at $\varepsilon \approx 0.5\%$. In **c)**, the dashed lines are extrapolations of the excess free energy.

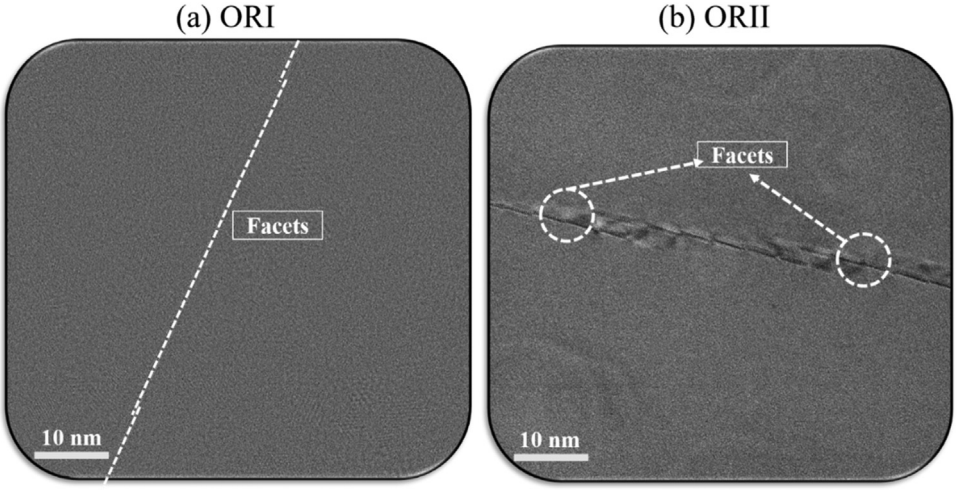

Fig. 8. BF-TEM images of asymmetric variants of Σ3 ($\bar{2}$11) GB from a) ORI and **b)** ORII, showing facets of varying length separated by steps. Small circle marked in b) shows the smaller facets incorporated by small steps within longer facets.

To gain deeper insights, we also tracked several excess properties as a function of ε: The excess energy $[U]$, the excess volume $[V]$, and the excess shear $[B_1]$. At $\varepsilon = 0$, the latter corresponds to the shift between the {111} planes in tilt axis direction across the GB (as indicated in Fig. 7a)). Positive and negative values of $[B_1]$ are equivalent in the case of Σ3 ⟨111⟩ {112} tilt GBs in fcc: These lead to equivalent, if differently oriented, GB structures due to the bicrystal symmetry. The values of $[B_1]$ are of the same order of magnitude as in the experiment (Figs. 5 and 6), but due to the small magnitude of the shift and the unknown stress state as well as measurement uncertainty in the experiment, a quantitative comparison is not possible. We also calculated the GB free energy, which is $\gamma = [U] - \sigma_{33}[V]$ in this case [17,18], and the angle α as defined in Fig. 4. All values are shown in Fig. 7c)–f). We can see that there is a jump in the excess values and a discontinuity in the excess free energy at $\varepsilon \approx 0.5\%$. This indicates that |E| and |E'| are indeed distinct microstates. The reason for the transformation between the two states is that the atomic arrangement in |E'| leads to a larger excess volume, which becomes favorable under tension.

3.5. Asymmetric variants of Σ3 grain boundaries of ORI and ORII

The BF-TEM image in Fig. 8 shows the asymmetric variants of the Σ3 in two ORs. Both the ORs incorporate facets regularly interrupted by steps with varying heights in order to accommodate the overall deviation in grain boundary plane deflection from the symmetric orientation. We found that the GB from ORII has a greater number of facets and steps in comparison to ORI. This is also manifested microscopically in Figure S4 and S5 by using plane trace analysis in EBSD. The atomic structures of asymmetric variants of Σ3 are depicted in Figs. 9 and 10. In the case of ORI, the GB consists of long facets of 40 nm up to 60 nm in length separated by small steps with a step height of 0.3 nm, but no facet with larger step heights are found. Unlike ORII, the absence of larger steps in ORI is due to a small deviation (because of the change in GB curvature locally) of approximately 1.2° in GB plane inclination from the exact habit plane in comparison to a large deviation of 5.5° deviation for ORII. We experimentally observed that the symmetric facets are disrupted by isolated defects in order to compensate for the deviation in GB inclination. Thus, it is unlikely that they are responsible for the differently reconstructed GB structural unit, especially considering that the deviation angles are quite small.

In the case of Σ3 (11$\bar{2}$) GB from ORII, it consists of long facets of around 20 nm in length separated by steps with heights from 5 nm down to 1 nm. The longer facets are comprised of smaller facets of around 4 nm in length interrupted by steps with varying small step heights. The magnified view in the light blue and blue boxes in Fig. 9c) and 9d) indicates a GB step and shows that the core structure of the step is quite ordered. Also, no incorporation of additional subunits has been observed in any of the cases.

3.6. Dislocation characterization of GB steps

To analyze whether the steps present at the interface are associated with any secondary grain boundary dislocations or not, the Burgers circuit mapping method is adopted from Medlin et al. [40]. The Burgers vector **b**, of the interfacial steps can be determined as

$$\mathbf{b} = -\left(\mathbf{C}_\gamma + R\mathbf{C}_\beta\right). \tag{1}$$

Here, $\mathbf{C}_\gamma$ and $\mathbf{C}_\beta$ are the path of the Burgers circuit corresponding to the lattice translation vectors in the two grains (Grain γ and β) as shown in Figs. 10a) and 10b). R is a rotation matrix that converts a crystal reference system from grain γ to β, here representing a 60° rotation around the tilt axis:

$$R_{\Sigma 3} = \frac{1}{3}\begin{bmatrix} 2 & \bar{1} & 2 \\ 2 & 2 & \bar{1} \\ \bar{1} & 2 & 2 \end{bmatrix}$$

Circuit $\mathbf{C}_\gamma$ starts from A, follow B and ends at C while $\mathbf{C}_\beta$ path starts from D, follow E and ends at F in clockwise direction as shown in Fig. 10. The circuits are constructed in such a way that they converge at crystallographically equivalent sites on both sides of the facet, so that $\overline{AF} = -\overline{CD}$, cancelling out the unknown parts of the Burgers circuit.

We found that the steps present in both the ORs are associated with Burgers vectors as listed in Table 2 and the interfacial structure is identical on either side of the steps. Hence, it is clear that these steps shown in Figs. 9 and 10 are disconnections with varying heights (h), where both **b** and h are the translation vectors of the displacement shift complete (DSC) lattice.

In the case of Σ3 from ORI, only one kind of disconnection with Burgers vector $\mathbf{b}_1 = 1/6[\bar{1}\bar{1}2]$ and a step height of $2a_{dsc}$ (0.3 nm) is observed, where a_{dsc} is the lattice parameter of the DSC lattice. In ORII, disconnections with the same Burger vector, i.e. $\mathbf{b}_1 = 1/6[\bar{1}\bar{1}2]$, with different step heights of $2a_{dsc}$ (0.3 nm) and $5a_{dsc}$ (0.8 nm) are observed across the GB. The atomic structure of both types of disconnections look similar and quite ordered. We

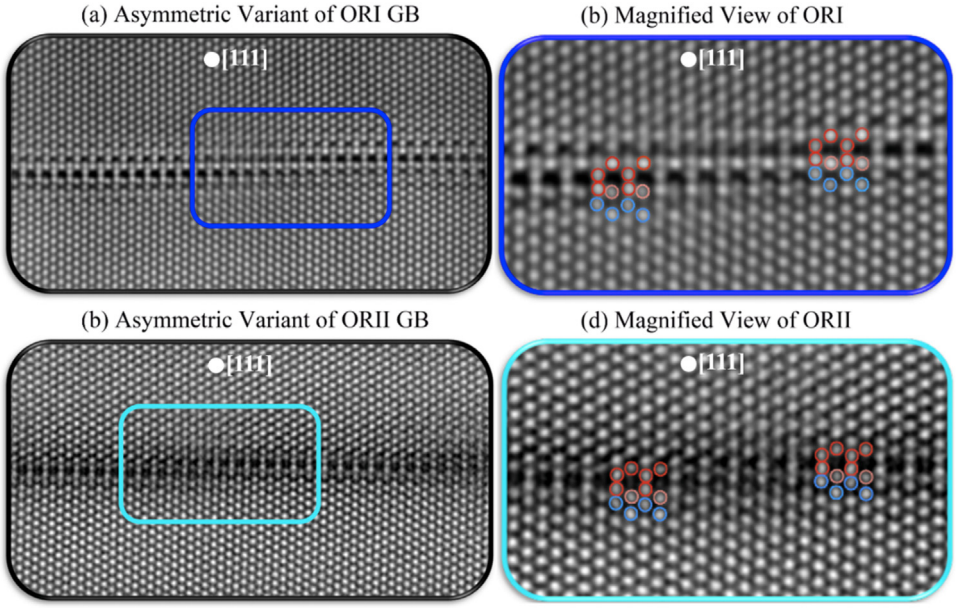

Fig. 9. STEM-HAADF images showing asymmetric variants of the GBs in plan-view along [111] zone axis orientation. a) Atomic structure of asymmetric variant of Σ3 ($11\bar{2}$) from ORI. **b)** Atomic structure of asymmetric variant of Σ3 ($11\bar{2}$) from ORII. The images depicted in **c)** and **d)**, as marked by blue and light blue boxes, show a close-up view of the GB step highlighted in **a)** and **b)**.

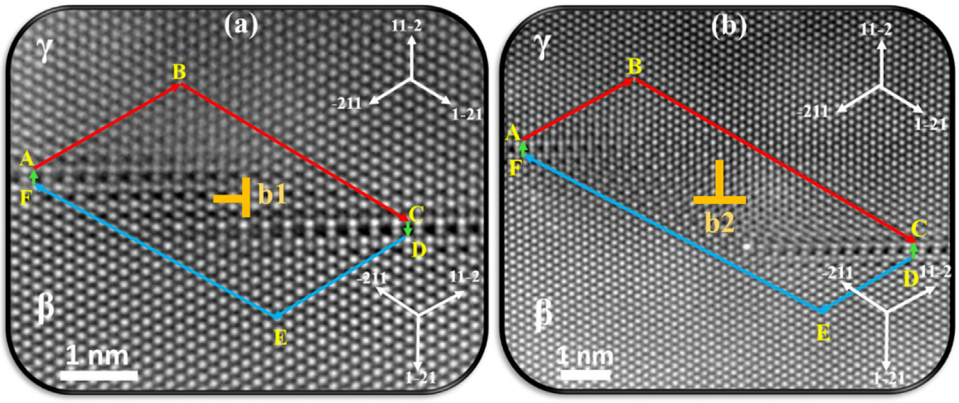

Fig. 10. STEM-HAADF images showing two different types of steps along [111] zone axis at the Σ3 ($11\bar{2}$) GB from ORII. a) Atomic structure of GB step type A with 0.8 nm length. **b)** Atomic structure of GB step type B with 3 nm length. Burgers circuits depicted in **a)** & **b)** start from position A in a clockwise direction and end at position F. The red lines (ABC) in grain γ and blue lines (DEF) in grain β represent the upper and lower part of the Burgers circuit. As summarized in Table 2, the Burgers circuits in **a)** and **b)** give $\mathbf{b}_1 = 1/6[\bar{1}\bar{1}2]$ and $\mathbf{b}_2 = 1/2[\bar{1}01]$, respectively.

Table 2
Burgers vectors b determined using Eq. (1) for the circuit maps constructed around pairs of facet junctions in ORII as shown in Fig. 10. The values of the two half-circuit $\mathbf{C}_\gamma$ and $\mathbf{C}_\beta$ are also provided, alongside the step height h.

Type of steps	C_γ:ABC (Grain γ)	C_β:DEF (Grain β)	b (Burgers vector)	h (Step height)
Type A	1/6 [46 $\overline{55}$ 8]	1/6 [$\overline{56}$ 10 46]	1/6 [$\bar{1}\bar{1}2$]	0.8 nm
Type B	1/6 [69 $\overline{93}$ 24]	1/6 [$\overline{93}$ 27 66]	1/2 [$\bar{1}0\bar{1}$]	3.0 nm

also found another type of disconnection with a different Burgers vector $\mathbf{b}_2 = 1/2[\bar{1}01]$ and a step height of approximately 3 nm as shown in Fig. 10b). The distribution of two distinct types of GB dislocations associated with different steps, recognized in the [111] Σ3 from both ORs is illustrated in Fig. 11.

It is important to take into account that in addition to the deviation in GB plane inclination, deviation in the misorientation is also responsible for accommodating the disconnection kind of defects at the GB. In the case of ORI (for a longer segment including the disconnection with a Burgers vector $\mathbf{b}_1 = 1/6[\bar{1}\bar{1}2]$), we have approximately 1° of deviation from the ideal 60° misorientation. This average value of 1° deviation is estimated by using the lines along the planes on both the grains forming the GB and then measuring the angles between the drawn lines. However, when we zoom in locally, we have ideal 60° misorientation for the perfect Σ3 symmetric segment without any disconnection (see Fig. 3). This clearly indicate that the deviation in the misorientation of the GB is compensated by the introduction of defects like disconnections. Likewise, in ORII (for a longer facets with disconnections corresponding to a Burgers vector of $\mathbf{b}_1 = 1/6[\bar{1}\bar{1}2]$), we have a deviation of ∼2.3° in the misorientation for the longer facets, associated with an average spacing of 4.1 nm approximately. While locally, we have a deviation of 1° from the ideal misorientation for the perfect symmetric segment (see Fig. 3). Therefore, globally, both

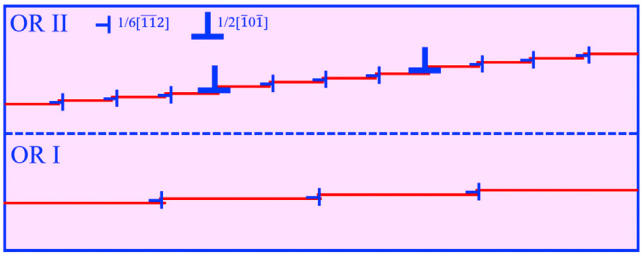

Fig. 11. Schematic illustration of the distribution of two different types of grain boundary dislocations ($\mathbf{b}_1 = 1/6[\bar{1}\bar{1}2]$ and $\mathbf{b}_2 = 1/2[\bar{1}01]$) associated with different steps observed along the incoherent $\Sigma 3$ ($\bar{2}11$) GBs from ORI and ORII.

the deviation in GB misorientation and the GB plane inclination are responsible for incorporating the $\mathbf{b}_1 = 1/6[\bar{1}\bar{1}2]$) and/or $\mathbf{b}_2 = 1/2[\bar{1}01]$ disconnections at the GB. Moreover, it is very likely that the facets between the disconnections are the remainders of GB migration that occurred at high temperatures during the annealing of the film. Although no pure steps (without any dislocation character) are found in the GBs examined, there is also a possibility that pure steps may have been incorporated into the GBs instead of disconnections in order to compensate a deviation in GB plane inclination.

The aforementioned two different disconnections having the same Burgers vector $\mathbf{b}_1 = 1/6[\bar{1}\bar{1}2]$ and different heights can be explained with the help of a schematic illustration of disconnection formation in Fig. 12. A dichromatic pattern is formed by overlaying the two [111] lattices A and B, which are rotated by 60° w.r.t to each other as demonstrated in Fig. 12a). The pristine GB structure of $\Sigma 3$ [111] {112} can be obtained by eliminating the lattice points from the respective lattices on each side of the GB plane (see Fig. 12b)). The CSL and DSC lattices emerging from the dichromatic pattern for the $\Sigma 3$ [111] boundary are displayed in Fig. 12c). Furthermore, translation of the lattice B relative to lattice A by a DSC vector relocates the CSL origin and the boundary plane to a new site (Fig. 12d) - 12f)). This results in the incorporation of a disconnection at the GB with a Burgers vector of $\mathbf{b} = 1/6[\bar{1}\bar{1}2]$ and a step height h. As equivalent locations of the GB plane in the shaded region exist, multiple disconnections with the same Burgers vector but different step height are possible, each with a different energy [25]. The two disconnections observed experimentally (in Fig. 9 and 10) are shown schematically in Fig. 12e) & 12f). Both disconnections have the same Burgers vector but different step heights $2a_{dsc}$ and $5a_{dsc}$.

4. Discussion

4.1. Atomic structure and excess properties

While the symmetric $\Sigma 3$ [111] ($11\bar{2}$) GBs with OR I and OR II have the same macroscopic DOFs, the GBs exhibit two different microstates with subunits |E| (distorted hexagonal units) and |E'| (perfect hexagonal units). The |E'| structural unit was already predicted using atomistic simulations by Sutton et al. [23], however, that work does not contain the experimentally observed |E| motifs. In copper, Wang et al. [22] simulated two different structures with |F| (stable) and |F'| (metastable) units. The |F| motif bears some resemblance to the experimentally observed structure in Al, although the angles and interatomic distances do not match. It is important to note that these simulations used simple pair potentials, which are not capable of fully describing the physics of metals. Later, Hetherington et al. [41] combined both the atomistic simulation and the atomic resolution TEM to investigate the atomic structure of $\Sigma 3$ [111] ($11\bar{2}$) facets of the incoherent twin GBs in gold (Au). It was identified that there was no one-to-one correlation between the simulated and the experimental images due to the lower resolution limit of the microscope. On closer comparison of the atomic structure of the GBs in Au with Al, we found that both the experimental and the simulated motifs in Au does not match with any of the motifs present in Al. We therefore investigated the structures with aberration corrected STEM and performed the simulations with a more realistic EAM potential in this work. Furthermore, we also verified the results using DFT simulations. We found that the |E| structure transforms into the |E'| structure when applying a stress or strain in the plane parallel to the substrate. The reason for this is that the GB excess volume couples to stresses applied normal to the GB plane (σ_{33}), resulting in a GB free energy of $\gamma = [U] - \sigma_{33}[V]$. The |E'| motif has a higher excess volume and thus occurs under tension. Because neither variant is mechanically (meta-)stable concurrently with the other variant, both motifs can only be observed by applying stress or strain, which explains why these microstates were not found in earlier simulations.

High-resolution STEM imaging of the cross-sectional view along the ⟨110⟩ zone axis reveals that there is a slight shift of the {111} planes across the GBs in both ORs. The farther the boundary gets away from the substrate, the higher is the magnitude of the shifts between the {111} planes. These rigid body translations during grain boundary relaxation usually occur in order to reduce the grain boundary energy [37,42] and were also predicted by our simulations. No such shifts are observed for the segments close to the substrate for both ORs. Various studies reported that the magnitude of these translations at the GB is very sensitive to the surroundings of the boundary (such as presence of triple junction, phase interface or defects near the GB) [43,44]. The presence of sapphire near this segment of the symmetric twin imposes a rigid frame on the GB that prevents the occurrence of any rigid body translations of {111} planes near the substrate. In addition, asymmetric twin facets are present along the ⟨110⟩ zone axis in ORII as compared to the perfectly planar GB observed in ORI. It is important to note that there is no dislocation character associated with these steps, unlike the disconnections observed from the [111] zone axis direction. Nevertheless, these facets indicate that the boundary might have migrated from left to right at elevated temperature during the annealing treatment.

Regarding the transition from |E| to |E'| motifs, the simulations predict that a planar strain of at least 0.5% is required. One possible origin for such a strain could be the difference in the thermal expansion coefficients, between the substrate (8.18×10^{-6} K^{-1} in the basal plane) and the film (23.1×10^{-6} K^{-1}) [45,46]: $\varepsilon = \Delta\alpha \times 400$ K = 0.6%. However, this does not explain the difference between the ORI and ORII motifs. Another possibility could be the different lattice mismatch between Al film and the sapphire substrate for ORI and ORII. Medlin et al. [38] considered the lattice parameter of sapphire and employed the lattice coincidence relationships analysis method [47] to calculate the lattice mismatch between Al and sapphire substrate in ORII and estimated it to be −4.3% for ORI and +0.4% for ORII. On the other hand, Hieke et al. [48] used the lattice plane spacing values directly to calculate the lattice mismatch and found it to be −4.3% for ORI and −20% for ORII. These results contradict each other and only the approach by Medlin et al. fits qualitatively to the simulations, which predict |E| units occur under compression/slight tension and |E'| units under larger tension ($\varepsilon > 0.5\%$). According to the literature [38,49], the value of the lattice misfit parameter can be estimated by using different approaches, depending on the elastic properties of the materials. However, it should be noted that all the above-mentioned approaches for the lattice strain calculations are relatively simple and imprecise. For instance, delocalized coherency, i.e. a local rearrangement of the atoms at the interface, may result in a reconstructed interface structure [50] that reduces the interface energy.

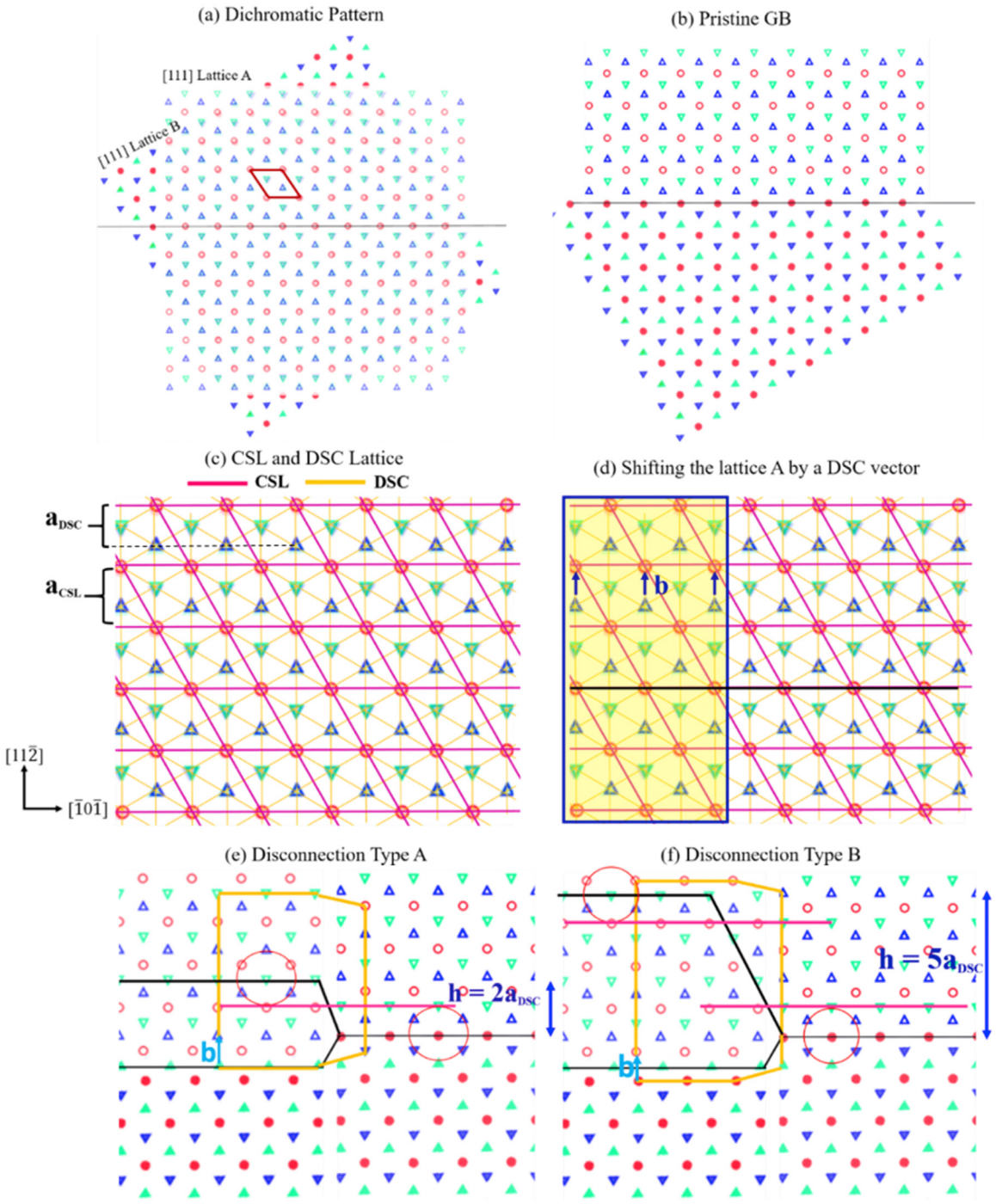

Fig. 12. Schematic illustration of the disconnection defects in an incoherent Σ3 [111] symmetric tilt GB. a) Dichromatic pattern obtained by overlaying two lattices oriented along [111] direction: lattice A and lattice B (rotated by 60° relative to lattice A) containing filled and unfilled lattice points, respectively. The green, blue and red layers in both lattices indicate the typical (111) ABCABCABC… fcc stacking sequence. A new super lattice structure emerges due to concurrent lattice points (light red lattice points), called coincidence sites lattice (CSL). **b)** The pristine GB structure of Σ3 [111] with a GB plane of (211) is indicated by the black line. The pink and yellow lines in **c)** represent CSL and DSC lattice vectors, respectively. **d)** A shift of the lattice B relative to the lattice A by a DSC vector $\mathbf{b} = 1/6[\bar{1}\bar{1}2]$ indicated by blue arrows in the yellow region, relocates the origin of the CSL lattice and the boundary plane (black line). This leads to the formation of a disconnection with a Burgers vector $\mathbf{b} = 1/6[\bar{1}\bar{1}2]$ along the GB. **e)** and **f)** show the two kinds of disconnections associated with step heights $h = 2a_{dsc}$ and $h = 5a_{dsc}$ for the same Burgers vector **b**. Yellow lines depict the Burgers circuit around the disconnections. Pink circles in **e)** and **f)** represent structural units corresponding to the pristine GB structure.

The possibility of interface reconstruction makes these purely geometrical models questionable. Nevertheless, the observed atomic structures of the Σ3 [111] GBs from both simulation and experiments are in excellent agreement with each other and paved a useful insight into the understanding the influence of grain boundary structure multiplicity on the properties of the delimiting Σ3 [111] tilt boundaries in Al.

4.2. Disconnections in Σ3 [111] GBs

The occurrence of different types of Σ3 [111] disconnections with Burgers vector $\mathbf{b}_1 = 1/6[\bar{1}\bar{1}2]$ and $\mathbf{b}_2 = 1/2[\bar{1}01]$ with varying heights in both ORs is attributed to the substantial deviation in the misorientation and the GB plane inclination from the symmetric orientation. To the authors' knowledge, this is the first time

that the atomic-scale experimental observations of GB disconnections in incoherent Σ3 [111] tilt GBs in pure Al are being reported. Numerous studies [29,31,32] show that the GB kinetics are highly controlled by the dynamics of disconnections, such as the nucleation and the propagation of disconnections along with the GB in a polycrystalline material. The experimentally observed large number disconnections at the Σ3 [111] GBs could indicate the nucleation and propagation of these disconnections and steps at the GB from the triple junctions during annealing. The motion and annihilation of these disconnections may have contributed differently to the GB migration at high temperatures. However, it is difficult to elaborate globally whether all these facets or disconnections already existed due to a deviation from exact CSL misorientation/habit plane or nucleated from the triple junctions at elevated temperatures. Nevertheless, the existence of only one type of disconnection in ORI may suggest the possibility of a lower migration rate for ORI in comparison to ORII, where more than one type of disconnection is observed. However, for quantitative study of the energies of these disconnections and their effect on the mechanism of GB migration, more studies such as in-situ annealing experiments in combination with in-depth simulations are needed which is beyond the scope of the current article.

5. Conclusion

In the present work, a detailed systematic study is conducted to investigate the structure multiplicity and structural defects in incoherent Σ3 [111] $(11\bar{2})$ tilt GBs using aberration corrected high-resolution transmission electron microscopy technique. Furthermore, MD and DFT simulations are utilized to understand the impact of the two different microstructural states of two ORs on GB properties. We found two different microstates, |E| and |E'|, of the GB structure. Simulations predict that these states transform into each other with applied stress or strain by coupling to the different excess volume of the microstates. |E| motifs were associated with GBs with ORI and |E'| motifs with ORII. This suggests that these microstates are the result of different strain states due to different local stress states present at the interfaces. Also, the atomic structure of both the GBs along ⟨110⟩ zone axis is investigated in detail with HAADF-STEM. Different magnitudes of translation of {111} planes are observed across the whole GB from the bottom near the substrate up to the surface of the Al film, for both ORs. The asymmetric variants of the GBs at the two ORs incorporate different types and density of facets into the structure of Σ3 GB. In case of Σ3 from ORI, GB consists of long facets separated by small steps with a single step height of typically 0.3 nm. However, Σ3 from of ORII comprises of a large number of facets incorporating different kind of disconnections with varying step height. The ORII GB exhibit two different types of disconnections with Burgers vector $1/6[\bar{1}\bar{1}2]$ and step height $h = 2a_{\mathrm{dsc}}$ and $5a_{\mathrm{dsc}}$, while for ORI only a single disconnection type with step height $h = 2a_{\mathrm{dsc}}$ is observed. Furthermore, in ORII, another type of disconnection with Burgers vector $1/2[\bar{1}01]$ and varying step heights were found in contrast to absence of such disconnections in ORI. This suggests the possibility of a lower migration rate in ORI in comparison to ORII, where more than one type of disconnections are observed.

Data availability

The main datasets of this study are published at https://doi.org/10.5281/zenodo.6414955. Other data supporting the findings of this study are available from the authors upon reasonable request.

Declaration of Competing Interest

The authors declare that they have no known competing financial interests or personal relationships that could have appeared to influence the work reported in this paper.

Acknowledgments

This project has received funding from the European Research Council (ERC) under the European Union's Horizon 2020 research and innovation program (Grant agreement No. 787446; GB-CORRELATE).

Supplementary materials

Supplementary material associated with this article can be found, in the online version, at doi:10.1016/j.actamat.2022.118499.

Appendix

Appendix A. Validation and comparison of EAM potentials

The validity of the predictions of the atomistic computer simulations depends on the interatomic potential. We compared three different EAM potentials for Al [35,51,52]: Mishin et al. (1999), Liu et al. (2004), and Mendelev et al. (2008). For each potential, the lattice constant and cohesive energy at 0 K were calculated. Then, we performed the γ-surface search as described in the methods section. We also tested this with two other potentials [53,54], but found that numerical problems lead to wildly fluctuating or even very large negative GB energies. We thus did not further investigate these potentials. In the remaining simulations, we always found structures that resembled either the |E| or |E'| motifs. The excess properties at $T = 0$, $\sigma = 0$, and $\varepsilon = 0$ are listed in Table A.1.

Since we found that the potentials differ significantly in the expected ground-state motif, as well as in the excess properties, we additionally performed density functional theory (DFT) calculations using VASP 5.4.4 [55–58]. For this, we prepared a smaller simulation cell with 72 atoms, dimensions of around $7 \times 2 \times 60$ Å^3, and full periodic boundary conditions, resulting in two identical grain boundaries in the cell. We also set up an equivalent reference structure containing no grain boundaries. The simulations were set up and analyzed using pyiron [59]. We employed the projector-augmented wave (PAW) method [60] within the generalized gradient approximation (GGA) with the Perdew–Burke–Ernzerhof (PBE)

Table A.1
The theoretical values of different excess properties at $T = 0$, $\sigma = 0$, and $\varepsilon = 0$ for different potentials and DFT calculations are listed. Here, a and E_{coh} are the fcc lattice constant and cohesive energy; γ_0, $[V]$, $[\tau i_j]$ represent the GB energy, excess volume and GB stress tensor values, where $(i, j = 1,2)$. The angle α is defined in Fig. 7(a). $[B_1]$ and $[B_2]$ are the components of the microscopic translation vector between the two crystallites in the GB plane.

	DFT	Mishin et al. (1999)	Liu et al. (2004)	Mendelev et al. (2008)	
a	4.040	4.050	4.032	4.045	Å
E_{coh}	–	−3.36	−3.36	−3.41	eV/atom
motif	|E|	|E|	|E'|	|E|	
γ_0	0.390	0.355	0.322	0.418	J/m²
$[V]$	0.258	0.288	0.480	0.414	Å
α	151°	151°	126°	143°	
$[B_1]$	±0.350	±0.351	±0.780	±0.266	Å
$[B_1]\cdot\sqrt{3}\ /a$	±0.150	±0.150	±0.335	±0.114	
$[B_2]$	±1.428	±1.432	±1.426	±1.430	Å
$[B_2]\cdot\sqrt{2}\ /a$	±0.5	±0.5	±0.5	±0.5	
$[\tau_{11}]$	–	0.94	1.85	0.78	J/m²
$[\tau_{22}]$	–	0.50	0.50	0.95	J/m²
$[\tau_{12}]$	–	0.00	0.00	0.00	J/m²

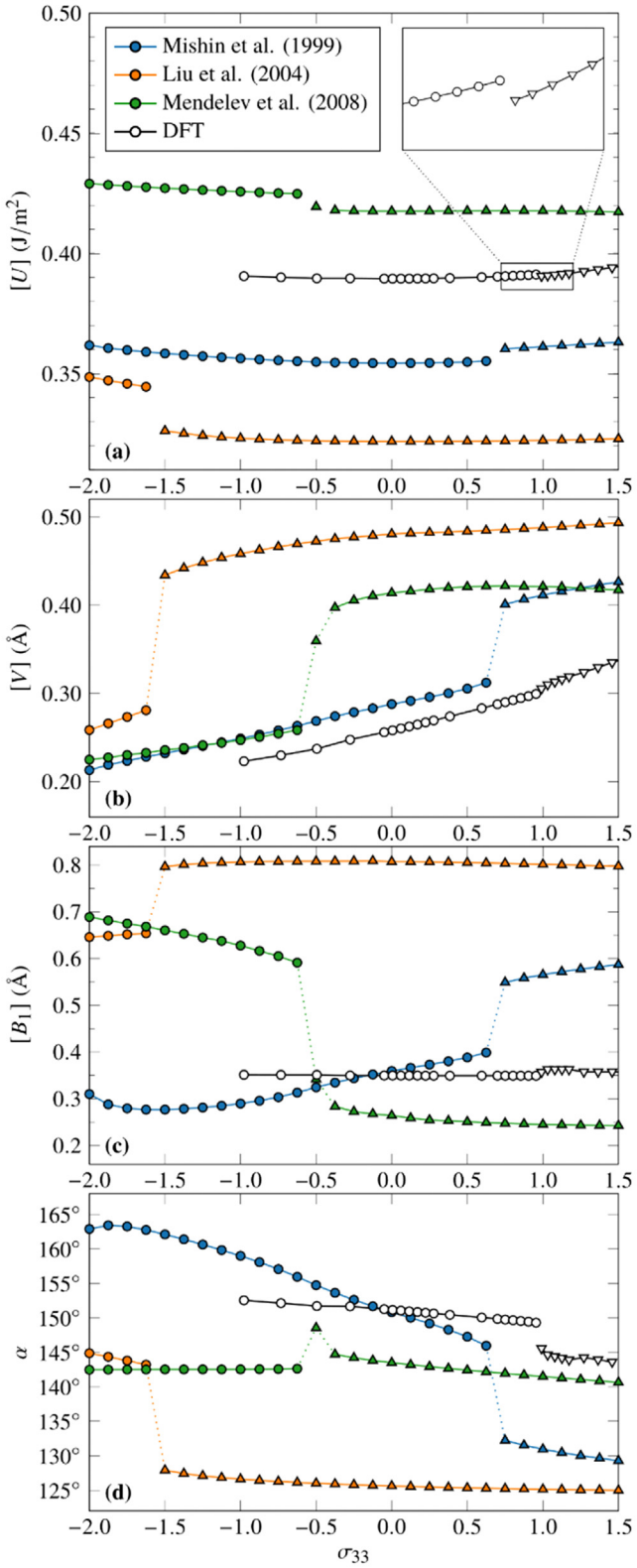

Fig. 13. Comparison of different excess properties calculated with DFT simulations and EAM potentials. Data points represent either |E| units (OR I, circles) or |E'| units (OR II, triangles). The changes are less pronounced in the DFT simulations than in the EAM potentials, but the potential by Mishin et al. [35] matches quite well in the stress-free state and most closely reproduces the stress required for the transformation from |E| to |E'|.

parametrization [61]. The PAW potentials [62] used three valence electrons ($3s^2 3p^1$) for Al.

Due to the sensitivity of GB excess properties to numerical errors, we used high-accuracy parameters for the DFT simulations. First, the Al lattice constant was determined using a cubical fcc unit cell to be 4.040(5) Å using a plane-wave energy cutoff of 450 eV and a 19 × 19 × 19 k-point mesh on a Γ-centered Monkhorst–Pack grid [63]. The GB simulations used the same parameters, except for a 27 × 27 × 2 k-point mesh. The equilibrium excess energy and volume at 0 K was found by scaling the box normal to the grain boundary planes, fitting a third order polynomial to the total energy as a function of the box length, and finding the minimum of that function. Stresses obtained by DFT and by the derivative of the energy agreed quite well due to the high accuracy of the simulations (very small Pulay stress). We therefore used the stresses calculated by VASP directly. Then, excess energy, volume, $[B_1]$, and α as a function of σ_{33} (the external stress normal to the GB plane) were computed as described in Ref. [17] using the defect-free reference system at corresponding σ_{33} values (Fig. 13). The GB excess stresses $[\tau_{ij}]$ were strongly affected by even very small residual stresses of the reference system and we regard them therefore as unreliable. We find that all potentials deviate qualitatively from the DFT results, especially at finite stresses. This is expected, since such empirical potentials are often only fitted to undeformed structures. Nevertheless, the potential by Mishin et al. (1999) [35] reproduces the ground state values quite well and is the only potential that captures the fact that the transformation from |E| to |E'| units occurs at tensile stresses on the order of 1 GPa. We therefore used this potential for the work described in the main text.

References

[1] P. Lejček, Grain Boundary Segregation in Metals, Springer Series in Materials Science 136, 2010 http://dx.doi.org/10.1007/978-3-642-12505-8.

[2] T. Frolov, D.L. Olmsted, M. Asta, Y. Mishin, Structural phase transformations in metallic grain boundaries, Nat. Commun. 4 (2013) 1–7, doi:10.1038/ncomms2919.

[3] W. Krakow, Structural multiplicity observed at a Σ = 5/[001]53·1° tilt boundary in gold, Philos. Mag. A Phys. Condens. Matter, Struct. Defects Mech. Prop. 63 (1991) 233–240, doi:10.1080/01418619108204847.

[4] T. Meiners, J.M. Duarte, G. Richter, G. Dehm, C.H. Liebscher, Tantalum and zirconium induced structural transitions at complex [111] tilt grain boundaries in copper, Acta Mater 190 (2020) 93–104, doi:10.1016/j.actamat.2020.02.064.

[5] E.W. Hart, Two-dimensional phase transformation in grain boundaries, Scr. Metall. 2 (1968) 179–182, doi:10.1016/0036-9748(68)90222-6.

[6] J.W. Cahn, Transitions and Phase Equilibria Among Grain Boundary Structures, J. Phys. (Paris), Colloq 43 (1982) 199–213, doi:10.1051/jphyscol:1982619.

[7] T. Meiners, T. Frolov, R.E. Rudd, G. Dehm, C.H. Liebscher, Observations of grain-boundary phase transformations in an elemental metal, Nature 579 (2020) 375–378, doi:10.1038/s41586-020-2082-6.

[8] L. Frommeyer, T. Brink, R. Freitas, T. Frolov, G. Dehm, C.H. Liebscher, Dual phase patterning during a congruent grain boundary phase transition in elemental copper, Nat. Commun. 13 (2022) 1–11, doi:10.1038/s41467-022-30922-3.

[9] G.H. Bishop, B. Chalmers, A coincidence - Ledge - Dislocation description of grain boundaries, Scr. Metall. 2 (1968) 133–139, doi:10.1016/0036-9748(68)90085-9.

[10] Q. Zhu, A. Samanta, B. Li, R.E. Rudd, T. Frolov, Predicting phase behavior of grain boundaries with evolutionary search and machine learning, Nat. Commun. 9 (2018), doi:10.1038/s41467-018-02937-2.

[11] S.J. Dillon, M. Tang, W.C. Carter, M.P. Harmer, Complexion: a new concept for kinetic engineering in materials science, Acta Mater 55 (2007) 6208–6218, doi:10.1016/j.actamat.2007.07.029.

[12] G. Duscher, M.F. Chisholm, U. Alber, M. Rühle, Bismuth-induced embrittlement of copper grain boundaries, Nat. Mater. 3 (2004) 621–626, doi:10.1038/nmat1191.

[13] T. Frolov, Y. Mishin, Phases, phase equilibria, and phase rules in low-dimensional systems, J. Chem. Phys. (2015) 143, doi:10.1063/1.4927414.

[14] M. Tang, W.C. Carter, R.M. Cannon, Diffuse interface model for structural transitions of grain boundaries, Phys. Rev. B - Condens. Matter Mater. Phys. 73 (2006) 1–14, doi:10.1103/PhysRevB.73.024102.

[15] P.R. Cantwell, M. Tang, S.J. Dillon, J. Luo, G.S. Rohrer, M.P. Harmer, Grain boundary complexions, Acta Mater 62 (2014) 1–48, doi:10.1016/j.actamat.2013.07.037.

[16] P.R. Cantwell, T. Frolov, T.J. Rupert, A.R. Krause, C.J. Marvel, G.S. Rohrer, J.M. Rickman, M.P. Harmer, Grain Boundary Complexion Transitions, Annu. Rev. Mater. Res. 50 (2020) 465–492, doi:10.1146/annurev-matsci-081619-114055.

[17] T. Frolov, Y. Mishin, Thermodynamics of coherent interfaces under mechanical stresses. II. Application to atomistic simulation of grain boundaries, Phys. Rev. B - Condens. Matter Mater. Phys. (2012) 85, doi:10.1103/PhysRevB.85.224107.

[18] T. Frolov, Y. Mishin, Thermodynamics of coherent interfaces under mechanical stresses. I. Theory, Phys. Rev. B - Condens. Matter Mater. Phys. 85 (2012) 12–15, doi:10.1103/PhysRevB.85.224106.

[19] A.P. Sutton, R.W. Baluffi, in: Interfaces in Crystalline Materials, Cladernon Press, Oxford, 1995, p. 1995. https://global.oup.com/academic/product/interfaces-in-crystalline-materials-9780199211067?cc=de&lang=en.

[20] K. Cheng, L. Zhang, C. Lu, K. Tieu, Coupled grain boundary motion in aluminium: the effect of structural multiplicity, Sci. Rep. 6 (2016) 1–11, doi:10.1038/srep25427.

[21] R.W. Balluffi, A.P. Sutton, Why should we be interested in the atomic structure of interfaces? Mater. Sci. Forum. 207–209 (1996) 1–12, doi:10.4028/www.scientific.net/msf.207-209.1.

[22] G.J. Wang, A.P. Sutton, V. Vitek, A computer simulation study of <001> and <111> tilt boundaries: the multiplicity of structures, Acta Metall 32 (1984) 1093–1104, doi:10.1016/0001-6160(84)90013-0.

[23] A.P. Sutton, V. Vitek, On the structure of the structures of tilt grain boundaries in cubic metals: symmetric tilt boundaries 309 (1983) 1–36, doi:10.1098/rsta.1983.0020.

[24] M.A. Tschopp, S.P. Coleman, D.L. McDowell, Symmetric and asymmetric tilt grain boundary structure and energy in Cu and Al (and transferability to other fcc metals), Integr. Mater. Manuf. Innov. 4 (2015) 176–189, doi:10.1186/s40192-015-0040-1.

[25] J. Han, S.L. Thomas, D.J. Srolovitz, Grain-boundary kinetics: a unified approach, Prog. Mater. Sci. 98 (2018) 386–476, doi:10.1016/j.pmatsci.2018.05.004.

[26] W. Bollman, Crystal Defects and Crystalline Interfaces, Springer Science & Business Media, 1970, doi:10.1007/978-3-642-49173-3_12.

[27] A.H. King, D.A. Smith, The effects on grain-boundary processes of the steps in the boundary plane associated with the cores of grain-boundary dislocations, Acta Crystallogr. Sect. A. 36 (1980) 335–343, doi:10.1107/S0567739480000782.

[28] J.P. Hirth, R.C. Pond, Steps, dislocations and disconnections as interface defects relating to structure and phase transformations, Acta Mater 44 (1996) 4749–4763, doi:10.1016/S1359-6454(96)00132-2.

[29] K.L. Merkle, L.J. Thompson, F. Phillipp, Thermally activated step motion observed by high-resolution electron microscopy at a (113) symmetric tilt grain-boundary in aluminium, Philos. Mag. Lett. 82 (2002) 589–597, doi:10.1080/0950083021000038074.

[30] E. Hosseinian, M. Legros, O.N. Pierron, Quantifying and observing viscoplasticity at the nanoscale: highly localized deformation mechanisms in ultrathin nanocrystalline gold films, Nanoscale 8 (2016) 9234–9244, doi:10.1039/c6nr00710d.

[31] A. Rajabzadeh, F. Mompiou, S. Lartigue-Korinek, N. Combe, M. Legros, D.A. Molodov, The role of disconnections in deformation-coupled grain boundary migration, Acta Mater 77 (2014) 223–235, doi:10.1016/j.actamat.2014.05.062.

[32] Q. Zhu, G. Cao, J. Wang, C. Deng, J. Li, Z. Zhang, S.X. Mao, In situ atomistic observation of disconnection-mediated grain boundary migration, Nat. Commun. 10 (2019) 1–8, doi:10.1038/s41467-018-08031-x.

[33] H.S. Nam, D.J. Srolovitz, Effect of material properties on liquid metal embrittlement in the Al-Ga system, Acta Mater 57 (2009) 1546–1553, doi:10.1016/j.actamat.2008.11.041.

[34] M. Schaffer, B. Schaffer, Q. Ramasse, Sample preparation for atomic-resolution STEM at low voltages by FIB, Ultramicroscopy 114 (2012) 62–71, doi:10.1016/j.ultramic.2012.01.005.

[35] Y. Mishin, D. Farkas, M.J. Mehl, D.A. Papaconstantopoulos, Interatomic potentials for monoatomic metals from experimental data and ab initio calculations, Phys. Rev. B - Condens. Matter Mater. Phys. 59 (1999) 3393–3407, doi:10.1103/PhysRevB.59.3393.

[36] S. Plimpton, Fast parallel algorithms for short-range molecular dynamics, J. Comput. Phys. 117 (1995) 1–19, doi:10.1006/jcph.1995.1039.

[37] G. Dehm, B.J. Inkson, T. Wagner, Growth and microstructural stability of epitaxial Al films on (0001) α-Al_2O_3 substrates, Acta Materialia 50 (2002) 5021–5032, doi:10.1016/S1359-6454(02)00347-6.

[38] D.L. Medlin, K.F. Mac Carty, R.Q. Hwang, S.E. Guthrie, M.I. Baskes, Orientation relationships in heteroepitaxial aluminium films on sapphire, Thin Solid Films 299 (1997) 110–114, doi:10.1016/S0040-6090(96)09393-5.

[39] G. Dehm, H. Edongué, T. Wagner, S.H. Oh, E. Arzt, Obtaining different orientation relationships for Cu films grown on (0001) α-Al_2O_3 substrates by magnetron sputtering, International Journal of Materials Research 96 (2005) 249–254, doi:10.3139/ijmr-2005-0045.

[40] D.L. Medlin, K. Hattar, J.A. Zimmerman, F. Abdeljawad, S.M. Foiles, Defect character at grain boundary facet junctions: analysis of an asymmetric $\Sigma = 5$ grain boundary in Fe, Acta Mater 124 (2017) 383–396, doi:10.1016/j.actamat.2016.11.017.

[41] C.J.D. Hetherington, U. Dahmen, R. Kilaas, A.I. Kirkland, A.R.R. Meyer, D.L. Medlin., HREM Analysis of Σ3 {112} Boundaries in Gold Bicrystal Films, in: EMAG Conf. Ser. Dundee, 2001, Philadelphia, 2001: p. vol. 168, pp. 59–62.

[42] R.C. Pond, V. Vitek, Periodic Grain Boundary Structures in Aluminium - 1. a Combined Experimental and Theoretical Investigation of Coincidence Grain Boundary Structure in Aluminium, Proc R Soc London Ser A 357 (1977) 453–470, doi:10.1098/rspa.1977.0179.

[43] H. Ichinose, Y. Ishida, N. Baba, K. Kanaya, Lattice imaging analysis of Σ3 coincidence-site-lattice boundaries in gold, Philos. Mag. A Phys. Condens. Matter, Struct. Defects Mech. Prop. 52 (1985) 51–59, doi:10.1080/01418618508237605.

[44] J.M. Pénisson, U. Dahmen, M.J. Mills, HREM study of a $\Sigma = 3\{112\}$ twin boundary in aluminium, Philos. Mag. Lett. 64 (1991) 277–283, doi:10.1080/09500839108214622.

[45] W.M. Haynes, D.R. Lide, T.J. Bruno, CRC Handbook of Chemistry and Physics, 97th, CRC Press/Taylor & Francis, 2016, doi:10.1201/9781315380476.

[46] W.M. Yim, R.J. Paff, Thermal expansion of AlN, sapphire, and silicon, J. Appl. Phys. 45 (1974) 1456–1457, doi:10.1063/1.1663432.

[47] C.A.M. Mulder, J.T. Klomp, On the internal structure of Cu- and Pt-sapphire interfaces, Le J. Phys. Colloq. 46 (1985) C4–111 No. C4 C4-11146, doi:10.1051/jphyscol:1985412.

[48] S.W. Hieke, B. Breitbach, G. Dehm, C. Scheu, Microstructural evolution and solid state dewetting of epitaxial Al thin films on sapphire (α-Al2O3), Acta Mater 133 (2017) 356–366, doi:10.1016/j.actamat.2017.05.026.

[49] A.E. Romanov, T. Wagner, On the universal misfit parameter at mismatched interfaces, Scr. Mater. 45 (2001) 325–331, doi:10.1016/S1359-6462(01)01035-1.

[50] H. Meltzman, D. Mordehai, W.D. Kaplan, Solid-solid interface reconstruction at equilibrated Ni-Al_2O_3 interfaces, Acta Mater 60 (2012) 4359–4369, doi:10.1016/j.actamat.2012.04.037.

[51] X.Y. Liu, F. Ercolessi, J.B. Adams, Aluminium interatomic potential from density functional theory calculations with improved stacking fault energy, Model. Simul. Mater. Sci. Eng. 12 (2004) 665–670, doi:10.1088/0965-0393/12/4/007.

[52] M.I. Mendelev, M.J. Kramer, C.A. Becker, M. Asta, Analysis of semi-empirical interatomic potentials appropriate for simulation of crystalline and liquid Al and Cu, Philos. Mag. 88 (2008) 1723–1750, doi:10.1080/14786430802206482.

[53] J.B. Sturgeon, B.B. Laird, Adjusting the melting point of a model system via Gibbs-Duhem integration: application to a model of aluminum, Phys. Rev. B - Condens. Matter Mater. Phys. 62 (2000) 14720–14727, doi:10.1103/PhysRevB.62.14720.

[54] X.W. Zhou, R.A. Johnson, H.N.G. Wadley, Misfit-energy-increasing dislocations in vapor-deposited CoFe/NiFe multilayers, Phys. Rev. B - Condens. Matter Mater. Phys. 69 (2004) 1–10, doi:10.1103/PhysRevB.69.144113.

[55] G. Kresse, J. Hafner, Ab initio molecular dynamics for liquid metals, Phys. Rev. B. 47 (1993) 558–561, doi:10.1103/PhysRevB.47.558.

[56] G. Kresse, J. Hafner, Ab initio molecular-dynamics simulation of the liquid-metal–amorphous-semiconductor transition in germanium, Phys. Rev. B. 49 (1994) 14251–14269, doi:10.1103/PhysRevB.49.14251.

[57] G. Kresse, J. Furthmüller, Efficiency of ab-initio total energy calculations for metals and semiconductors using a plane-wave basis set, Comput. Mater. Sci. 6 (1996) 15–50, doi:10.1016/0927-0256(96)00008-0.

[58] G. Kresse, J. Furthmüller, Efficient iterative schemes for ab initio total-energy calculations using a plane-wave basis set, Phys. Rev. B 54 (1996) 11169, doi:10.1103/PhysRevB.54.11169.

[59] J. Janssen, S. Surendralal, Y. Lysogorskiy, M. Todorova, T. Hickel, R. Drautz, J. Neugebauer, pyiron: an integrated development environment for computational materials science, Comput. Mater. Sci. 163 (2019) 24–36, doi:10.1016/j.commatsci.2018.07.043.

[60] P.E. Blöchl, Projector augmented-wave method, Phys. Rev. B. 50 (1994) 17953–17979, doi:10.1103/PhysRevB.50.17953.

[61] J.P. Perdew, K. Burke, M. Ernzerhof, Generalized gradient approximation made simple, Phys. Rev. Lett. 77 (1996) 3865–3868, doi:10.1103/PhysRevLett.77.3865.

[62] G. Kresse, D. Joubert, From ultrasoft pseudopotentials to the projector augmented-wave method, Phys. Rev. B - Condens. Matter Mater. Phys. 59 (1999) 1758–1775, doi:10.1103/PhysRevB.59.1758.

[63] H.J. Monkhorst, J.D. Pack, Special points for Brillonin-zone integrations, Phys. Rev. B. (1976) 2156–2164, doi:10.1103/PhysRevB.13.5188.